

Influence of Hopping Integrals and Spin–Orbit Coupling on Quantum Oscillations in Kagome Lattices

Xinlong Du¹, Yuying Liu¹, Chao Wang², and Juntao Song^{1*}

¹College of Physics and Hebei Advanced Thin Films Laboratory,
Hebei Normal University, Shijiazhuang, Hebei 050024, China

²College of Physics, Shijiazhuang University, Shijiazhuang, Hebei 050035, China
(Dated: March 9, 2026)

Motivated by recent experiments on CsTi₃Bi₅ and RbTi₃Bi₅ [Reh fuss *et al.*, Phys. Rev. Mater. **8**, 024003 (2024)], we theoretically investigate the effects of hopping integrals and spin-orbit coupling (SOC) on quantum oscillations in kagome lattice models. Our tight-binding models successfully capture the distinct quantum oscillation features observed in experiments, when a relatively strong SOC is included. It is more important that, by discussing the effect of the next-nearest-neighbor term t_2 , we provide a coherent explanation for their different topological responses. For the case of $t_2 = 0$, the small hybridization gap between adjacent bands with opposite Berry curvatures allows magnetic breakdown to occur under a strong magnetic field, enabling charge carriers to tunnel between the bands and thereby effectively masking the intrinsic topological character. In contrast, for $t_2 \neq 0$, the hybridization gap is significantly enlarged by t_2 , which suppresses magnetic breakdown and confines electrons to individual orbits with opposite Berry curvatures, thereby revealing the nontrivial Berry phase ($\phi_B \approx \pi$). Consequently, we identify the lattice-driven hopping t_2 as a critical control parameter that regulates the experimental observability of the topological phase in CsTi₃Bi₅ and RbTi₃Bi₅. These findings underscore the key role of the t_2 term and show that tuning lattice parameters can effectively control topological signatures in quantum transport.

I. INTRODUCTION

In condensed matter physics, the kagome lattice, with its unique band structure featuring Dirac points, van Hove singularities [1], and flat bands [2, 3], provides a rich playground for exploring emergent quantum phases and exotic behaviors [4, 5].

Quantum oscillation measurements have recently become a powerful probe of these unconventional properties in kagome lattice materials [6–8]. By measuring the oscillatory components of conductivity or resistivity as a function of the inverse magnetic field ($1/B$), one can directly access the Fermi surface geometry [9, 10] and extract key information about the underlying quantum states [11–14]. AV₃Sb₅ ($A = \text{K, Rb, Cs}$), a type of kagome lattice material, has attracted particular attention. In this quasi-two-dimensional kagome lattice structure, multiple electronic instabilities and pronounced quantum oscillations have been observed, which have been used to study its unique physical properties [15–29]. For instance, Dong *et al.* revealed the link between the anomalous Nernst effect and the topological electronic structure in CsV₃Sb₅ [30]. Zhang *et al.* identified the origin of ultra-high-frequency oscillations in the same compound [31]. Moreover, Shekhar *et al.* combined experiments and theoretical calculations to demonstrate the connection between topologically nontrivial band structure and charge density wave order in ScV₆Sn₆ [32].

More recently, Ti-based analogs ATi₃Bi₅ ($A = \text{Rb, Cs}$), another type of kagome lattice material, have drawn attention due to their distinct electronic characteristics [33–36]. Unlike AV₃Sb₅, ATi₃Bi₅ exhibits neither magnetism nor charge ordering [37, 38], offering a clean platform for probing intrinsic kagome physics through quantum oscillations [39, 40]. Li

et al., through calculating the quantum oscillation frequencies of ATi₃Bi₅, found pronounced three-dimensional features despite its quasi-two-dimensional Fermi surface geometry [41]. Subsequent measurements on CsTi₃Bi₅ confirmed a nontrivial Berry phase and topological band structure. At the same time, Ran *et al.* reported exceptionally high oscillation frequencies in CsTi₃Bi₅ and RbTi₃Bi₅, far exceeding those in conventional kagome metals [42].

Despite this progress, the electronic behavior of kagome lattices remains only partially understood. Quantum oscillations, as a direct probe of the Fermi surface, continue to provide crucial insights into the complex electronic structures of these materials. In general, systems with nearly identical band structures and Fermi surface geometries should present similar oscillatory behavior, since the extremal Fermi surface area A_F is directly related to the oscillation frequency F via the Onsager relation [43]:

$$F = \frac{\hbar}{2\pi e} A_F.$$

However, a recent experiment shows that CsTi₃Bi₅ and RbTi₃Bi₅, despite having nearly identical band structures and Fermi surface shapes, display strikingly different quantum oscillation spectra [42]. Lu *et al.* suggested that the Fermi surface of the Rb compound might deviate substantially from first-principles calculations due to the effects of doping, which can lead to different quantum oscillations.

Beyond doping effects, it is worth noting that even subtle modifications of hopping integrals can strongly influence quantum oscillations. Compared with doping-driven scenarios, this hopping-driven mechanism has received relatively little attention. In particular, variations in hopping integrals provide a microscopic mechanism that can produce distinct quantum oscillation spectra despite nearly identical electronic structures. Between RbTi₃Bi₅ and CsTi₃Bi₅, the difference in

* jtsong@hebtu.edu.cn

hopping terms arises from the variation in lattice constants: the smaller ionic radius of Rb^+ leads to a more compact lattice, where nearest-neighbor hopping dominates and longer-range hopping is negligible. In contrast, the larger ionic radius of Cs^+ causes the lattice to expand, weakening nearest-neighbor coupling and enhancing the importance of next-nearest-neighbor hopping. In this work, we propose another perspective: while the overall geometry of the Fermi surface is similar for the two materials, differences in hopping integrals can lead to subtle changes in orbital characteristics and effective mass, which in turn can result in distinct quantum oscillations.

We develop a theoretical framework to study how changes in hopping integrals influence quantum oscillation behavior in kagome lattices. The schematic of the model is shown in Fig. 1, where t denotes the nearest-neighbor hopping within the kagome layer, while t_1 and t_2 represent the nearest- and next-nearest-neighbor hoppings between the center site and the kagome sites, respectively. We focus on two representative cases: one with $t_2 = 0$, corresponding to RbTi_3Bi_5 , and the other with finite t_2 , relevant to CsTi_3Bi_5 . Although the overall band structures of these two cases are similar, distinct quantum oscillation spectra are observed in the two situations with different hopping. Through Fourier analysis and Landau-level fan diagrams, we demonstrate how modifications of the hopping integrals qualitatively alter the oscillation behavior. To more accurately simulate real materials, spin-orbit coupling (SOC) is included in both cases, and the resulting phase shifts are examined in detail. Our results show that subtle differences in hopping integrals can significantly reshape the quantum oscillation response, providing a self-consistent theoretical explanation for the experimentally observed differences between CsTi_3Bi_5 and RbTi_3Bi_5 .

The rest of this paper is organized as follows: In Sec. II, we introduce the theoretical models and their corresponding Hamiltonians, along with the methodology for calculating the density of states. Sec. III presents the numerical results. Finally, a summary is provided in Sec. IV.

II. THEORETICAL FRAMEWORK

Based on the kagome lattice structure, we construct a tight-binding model inspired by the crystal structures of CsTi_3Bi_5 and RbTi_3Bi_5 [42, 44, 45]. The corresponding lattice is shown in Fig. 1. In this model, the blue circles denote the kagome sites forming the basis of the kagome lattice, while the cyan circles at the hexagon centers represent additional sites introduced to capture key structural features of CsTi_3Bi_5 and RbTi_3Bi_5 . The tight-binding Hamiltonian is written as

$$H = H_0 + H_{\text{SOC}}, \quad (1)$$

$$H_0 = t \sum_{\langle ij \rangle} a_i^\dagger a_j + \left(t_1 \sum_{\langle ij \rangle} a_i^\dagger b_j + t_2 \sum_{\langle\langle ij \rangle\rangle} a_i^\dagger b_j \right) + \text{h.c.}, \quad (2)$$

$$H_{\text{SOC}} = i \frac{2\lambda}{\sqrt{3}} \sum_{\langle\langle ij \rangle\rangle} (\mathbf{d}_{ij}^1 \times \mathbf{d}_{ij}^2) \cdot \boldsymbol{\sigma} a_i^\dagger a_j, \quad (3)$$

where a_i and b_i denote the kagome basis sites and the additional center sites, respectively, corresponding to distinct sublattices of the lattice. In Eq. (2), the first term describes the nearest-neighbor hopping between kagome basis sites, while the second term accounts for hopping between the kagome basis sites and the center sites, with t_1 and t_2 denoting the nearest- and next-nearest-neighbor hopping integrals, respectively. The spin-orbit coupling term in Eq. (3) involves vectors \mathbf{d}_{ij}^1 and \mathbf{d}_{ij}^2 connecting second-nearest-neighbor sites in the kagome layer, where $\boldsymbol{\sigma}$ represents the Pauli matrices in spin space and λ is the SOC strength [46].

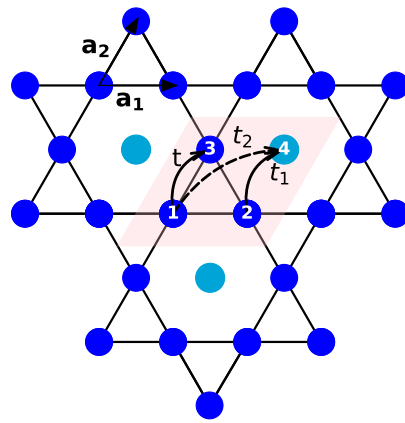


FIG. 1. (Color online) Schematic of the kagome lattice model with four sites (1, 2, 3, 4) per unit cell (pink shaded area). Nearest-neighbor vectors are $\mathbf{a}_1 = (1, 0)a$ and $\mathbf{a}_2 = (1/2, \sqrt{3}/2)a$, where a is the nearest-neighbor distance.

The density of states (DOS) is closely related to various physical quantities, such as the Pauli susceptibility and the resistivity. Quantum oscillations in the DOS necessarily give rise to oscillations in these quantities [47]. To calculate the zero-temperature DOS, we employ the Green's function formalism (see Appendix B for derivation):

$$\text{DOS}(E) = -\frac{1}{\pi} \text{Im}[\text{Tr} G]. \quad (4)$$

The Green's function of the central region, $G = (E - H)^{-1}$, is computed numerically using the recursive Green's function method [48, 49]. In particular, the diagonal blocks G_{ii} are obtained via the recursive Green's function method, enabling an efficient computation of the density of states. At finite temperatures, the oscillatory component of the DOS is described within the standard Lifshitz-Kosevich framework, which accounts for temperature-dependent effects. For a detailed discussion of the finite-temperature behavior, see Appendix C.

In numerical calculations, we consider a two-dimensional lattice of size $N_x = N_y = 60$. The hopping integrals are set to $t = -1$, $t_1 = -0.1$, and $t_2 = -0.01$. Quantum oscillations are

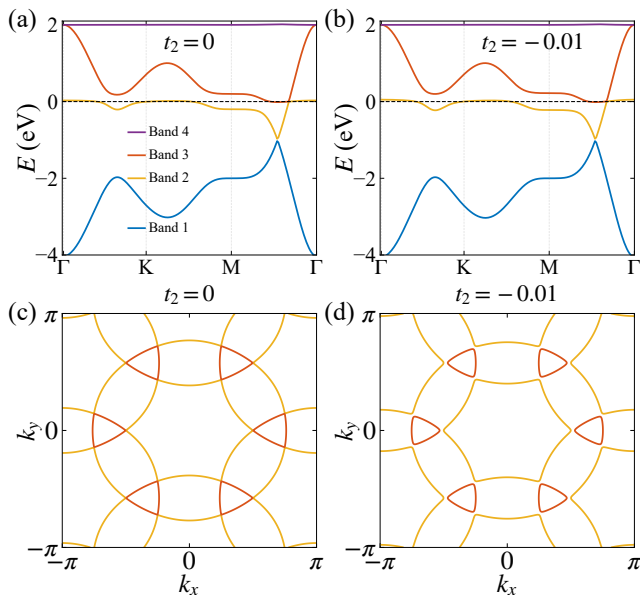


FIG. 2. (Color online) Band structures and Fermi surfaces for the two hopping mechanisms. The energy bands are indexed from bottom to top as Band 1, Band 2, Band 3, and Band 4. Panels (c) and (d) illustrate the Fermi surfaces taken at $E = 0$ corresponding to the band structures in (a) and (b), respectively. (a, c) Results for the $t_2 = 0$ case (nearest-neighbor hopping only). The Fermi surfaces in (c) originate from the crossing of Band 2 and Band 3 at the Fermi level. (b, d) Results for the $t_2 = -0.01$ case (including next-nearest-neighbor hopping). The SOC is set to $\lambda = 0$ for all panels.

computed without and with spin-orbit coupling, corresponding to $\lambda = 0$ and $\lambda = 0.05$, respectively. A perpendicular magnetic field B_{\perp} is incorporated into the system via a Peierls phase factor, $\phi_{ij} = \int_i^j \mathbf{A} \cdot d\mathbf{l} / \phi_0$, where $\mathbf{A} = (-yB_{\perp}, 0, 0)$ is the vector potential, and $\phi_0 = \hbar/e$ is the magnetic flux quantum [50, 51].

To investigate the band structures and Fermi surface geometries of the two cases, the momentum-space Hamiltonian $H(\mathbf{k})$ is derived via a Fourier transform, as detailed in Appendix A. Figure 2 presents the corresponding band dispersions and Fermi surfaces calculated using $H(\mathbf{k})$. We find that the band structures and Fermi surface geometries of the two cases are highly similar, capturing the similarity revealed by DFT calculations reported in experiments [42]. This similarity provides a suitable starting point for our subsequent analysis of the distinct quantum oscillation behaviors in the two cases.

III. NUMERICAL RESULTS

A. Capturing Key Experimental Signatures of Quantum Oscillations

To examine the effects of the two hopping mechanisms in kagome lattices, we computed and analyzed the DOS oscillations for the cases with $t_2 = 0$ and $t_2 = -0.01$. Figures 3(a) and 3(e) show the DOS oscillations as a function of inverse magnetic field $1/B$ for the two cases. Clear quantum oscilla-

tions are observed across the entire field range, with the case of $t_2 = -0.01$ showing more prominent frequency components than the case of $t_2 = 0$.

The discrete Fourier transform (FFT) of the oscillation signal as a function of magnetic field for both cases is calculated to analyze the oscillations, and the results are shown in Figures 3(b) and 3(f). We observe a single dominant frequency peak at 1898 T (γ) for the case of $t_2 = 0$. In contrast, for $t_2 = -0.01$, four fundamental frequency peaks appear at 249 T (α), 449 T (β), 1848 T (γ), and 2097 T (δ). The frequency spectrum for $t_2 = 0$ exhibits only a single peak (γ) around 2000 T, whereas the $t_2 = -0.01$ case shows multiple high-frequency components above 2000 T, most notably the δ peak at 2097 T. These calculated features align well with experimental observations.

The above analysis demonstrates that our model captures the key experimental distinction between RbTi_3Bi_5 and CsTi_3Bi_5 . Despite their highly similar band structures and Fermi surfaces [Fig. 2], the calculated quantum oscillations exhibit a striking difference: in the case of $t_2 = 0$, only a single oscillation frequency appears, akin to RbTi_3Bi_5 , whereas the case of $t_2 = -0.01$ produces a multi-frequency spectrum, mirroring the observations in CsTi_3Bi_5 . Crucially, the emergence of high-frequency components above 2000 T in this case ($t_2 = -0.01$) is a defining feature of CsTi_3Bi_5 that is absent in RbTi_3Bi_5 . Therefore, we conclude that the next-nearest-neighbor hopping t_2 is a key intrinsic parameter governing the distinct quantum oscillation behaviors in these materials.

Figures 3(c) and 3(g) present the Landau fan diagrams constructed for the γ -frequency peak for $t_2 = 0$ and $t_2 = -0.01$, respectively. The oscillation signal corresponding to the γ -frequency peak was isolated from the raw data using a numerical filter, and the filtered signal is plotted as a function of inverse field [Figs. 3(d) and 3(h)]. The maxima were assigned to $n + 1/2$, and the minima to $n + 1$. The intercept was then extracted by extrapolating the linear fits of the maxima and minima to zero inverse field. The intercept values obtained for the two cases are 0.047 for $t_2 = 0$ and 0.012 for $t_2 = -0.01$. Both intercept values are close to zero, indicating a trivial Berry phase in both cases. For a detailed explanation of how the Berry phase is determined from the intercept, see Appendix D.

In experiments, CsTi_3Bi_5 exhibits a nontrivial quantum phase shift, while RbTi_3Bi_5 shows no quantum phase shift. However, the current models yield no quantum phase shift both with and without t_2 . In other words, the spinless models are insufficient to reproduce the topological features observed experimentally. We attribute this discrepancy to the absence of spin-orbit coupling in the lattice models, as spin-orbit coupling is a crucial factor in driving topological phase transitions [52]. Therefore, it is necessary to incorporate spin-orbit coupling in both cases in subsequent analyses.

When SOC is included, the DOS oscillations, FFT spectra, and Landau fan diagrams for both cases are presented in Fig. 4. The amplitude of the DOS oscillations exhibits a significant enhancement compared to the spinless calculations in Figs. 4(a) and 4(e). This increase is primarily attributed to the explicit inclusion of the spin degree of freedom within the

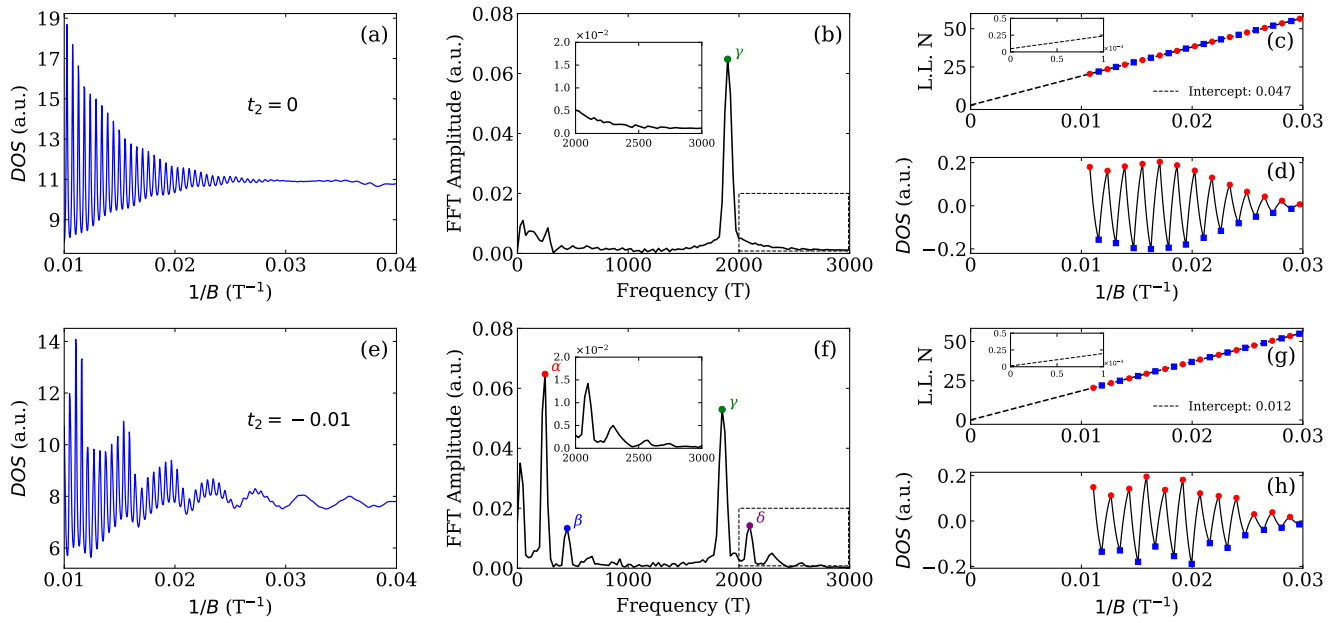


FIG. 3. (Color online) (a,e) DOS at $E_F = 0$ versus inverse magnetic field $1/B$ for the $t_2 = 0$ case (top) and $t_2 = -0.01$ case (bottom) without SOC. (b,f) Corresponding Fourier transform amplitudes versus frequency. (c,g) Landau fan diagrams plotting Landau level index N versus $1/B$ for the γ -frequency peak. (d,h) The main DOS oscillations versus $1/B$, with filters set between 1850–1900 T, to isolate the γ frequency contribution for constructing the Landau fan diagrams of the $t_2 = 0$ and $t_2 = -0.01$ cases, respectively.

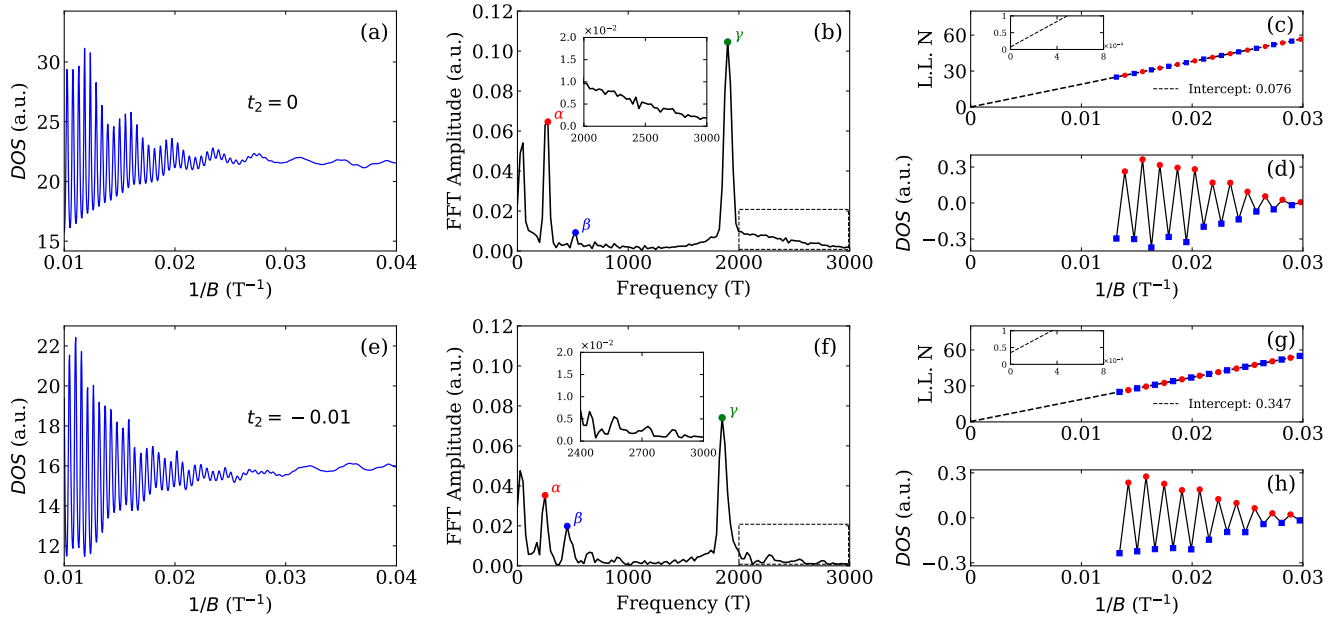


FIG. 4. (Color online) Same as Fig. 3, but with spin-orbit coupling strength $\lambda = 0.05t$. The DOS, Fourier transform amplitudes, and Landau fan diagrams are shown for the $t_2 = 0$ (top) and $t_2 = -0.01$ (bottom) cases, highlighting the effect of SOC on the Berry phase.

$2N \times 2N$ spinful Hamiltonian (where N denotes the spatial degrees of freedom), which accounts for the contributions from both spin channels. Clear quantum oscillations are observed across the entire field range for both cases, exhibiting similar frequency components in the raw data after the introduction of SOC. The FFT spectra for the corresponding cases are shown

in Figs. 4(b) and 4(f), where the characteristic frequency peaks α (249 T), β (449 T), and γ (1848 T) are identified in both patterns. In particular, in the $t_2 = -0.01$ case, multiple high-frequency peaks above 2000 T are observed under the effect of SOC, as clearly visible in the inset of Fig. 4(f). With the inclusion of SOC, the theoretical oscillations show excellent

agreement with the experimental data.

Landau fan diagrams for both cases with SOC are presented in 4(c) and 4(g). For the case of $t_2 = 0$, the phase analysis yields an intercept of approximately 0.076 [Fig. 4(c)], indicating that in the presence of SOC, the system remains topologically trivial. This result is consistent with the phase information reported for RbTi_3Bi_5 . For the case of $t_2 = -0.01$, after introducing SOC, the phase intercept increases to approximately 0.347 [Fig. 4(g)], which corresponds to a Berry phase close to π (since $2\pi \times 0.347 \approx 0.7\pi$). This corresponds to a non-trivial Berry phase of $\phi_B \approx 0.7\pi$ (derived via $2\pi \times \text{intercept}$), signaling that the electronic states at the Fermi level acquire a non-trivial topological character driven by SOC. Experimentally, CsTi_3Bi_5 is topologically non-trivial, while RbTi_3Bi_5 is topologically trivial. When SOC is included in the theoretical calculations for both materials, the results agree with the experimental data.

To sum up, by constructing a kagome lattice model with distinct hopping parameters, we successfully capture the contrasting quantum oscillation behaviors, despite the nearly identical band structures and Fermi surfaces. The key features extracted from our theoretical analysis align remarkably well with experimental findings for the two compounds. Specifically: (i) distinct quantum oscillation patterns; (ii) different FFT spectra, including the emergence of multiple high-frequency peaks above 2000 T for the case of $t_2 = -0.01$; (iii) distinct topological characteristics upon introducing SOC, with the $t_2 = -0.01$ case exhibiting a non-trivial Berry phase; and (iv) consistent thermodynamic damping behaviors, where the extracted effective masses ($m^* < m_0$) decrease upon introducing t_2 , reproducing the high-mobility character observed in experiments (see Appendix C for details). This comprehensive agreement confirms that the hopping-driven modification of the electronic structure provides a robust explanation for the distinct behaviors observed in CsTi_3Bi_5 and RbTi_3Bi_5 . Having established the validity of our model, we now turn to elucidating the underlying physical mechanism governing the topological observability.

B. Magnetic Breakdown and the t_2 -Induced Protection of Topological Signatures

The quantum oscillation analysis in Sec. III A has successfully captured the distinct frequency signatures of RbTi_3Bi_5 ($t_2 = 0$) and CsTi_3Bi_5 ($t_2 = -0.01$). However, a more profound distinction lies in their topological responses. The Landau fan diagrams reveal a trivial Berry phase for the case of $t_2 = 0$ but a non-trivial Berry phase for the case of $t_2 = -0.01$. To elucidate the physical origin of this discrepancy, we examine the electronic structures and highlight the pivotal role of SOC in determining the topological phase.

We first examine whether the difference in topological responses stems from the intrinsic band structures of the two cases. Figure 5 presents the calculated band structures and topological invariants for kagome nanoribbons with a fixed SOC strength ($\lambda = 0.05$). For the case of $t_2 = 0$ (Rb-like), a gap appears near $E \approx -1$ eV due to finite-size effects

[Fig. 5(a)]. Meanwhile, within the bulk gap opened by SOC, a pair of edge states, a hallmark of topological insulators, clearly emerges and crosses at the Dirac point. Similarly, for the case of $t_2 = -0.01$ (Cs-like) shown in Fig. 5(b), robust edge states are also observed crossing the gap. The topological nature is further quantified by the phase diagrams in Figs. 5(c) and (d). As the SOC strength λ increases, the bulk energy gap Δ_E opens linearly, and the Chern number C jumps discretely from 0 to ± 1 . This theoretical result confirms a crucial fact: both the Rb-like and Cs-like models are intrinsic topological insulators in the presence of SOC. This leads to a puzzling question: why do the quantum oscillation measurements for $t_2 = 0$ exhibit a topologically trivial signature, whereas those for $t_2 = -0.01$ display a topologically nontrivial one?

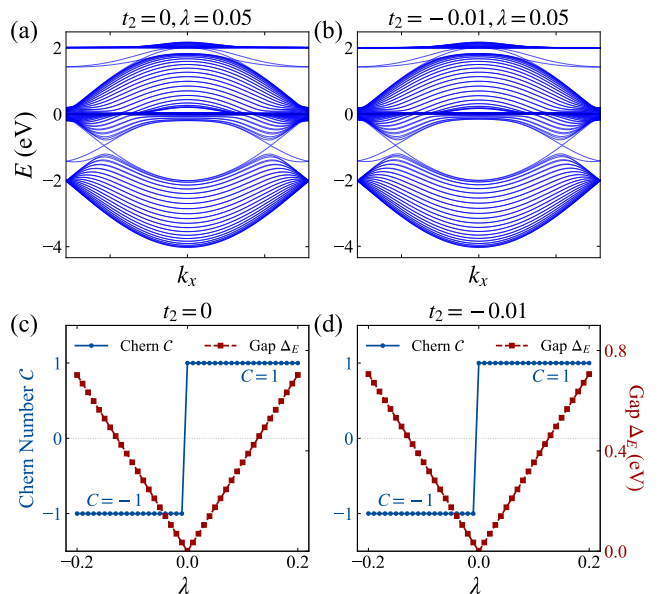


FIG. 5. (Color online) Calculated electronic structures and topological phase diagrams for $t_2 = 0$ and $t_2 = -0.01$. (a, b) Calculated nanoribbon band structures for (a) $t_2 = 0$ and (b) $t_2 = -0.01$ with fixed SOC strength $\lambda = 0.05$. Both cases exhibit gapless topological edge states crossing the bulk gap, indicating an intrinsically non-trivial topological phase. (c, d) Topological phase diagrams showing the evolution of the Chern number C (blue circles) and the bulk energy gap Δ_E (red squares) as a function of λ for (c) $t_2 = 0$ and (d) $t_2 = -0.01$. The persistent non-zero Chern number ($C = \pm 1$) confirms that both cases are topologically non-trivial in the bulk, despite differences in experimental quantum oscillation signatures.

To address this, we investigate the Fermi surface geometry at the Fermi level ($E_F = 0$), the energy scale probed by quantum oscillation measurements. The theoretical analysis is based on the effective k -space Hamiltonian derived in Appendix A. Figure 6 illustrates the evolution of the Fermi surface driven by the next-nearest-neighbor hopping t_2 . In the absence of t_2 [Fig. 6(a)], although SOC lifts the band degeneracy, the resulting gap is minimal, leaving the Fermi contours of Band 2 and Band 3 in close proximity. In contrast, introducing a finite $t_2 = -0.01$ [Fig. 6(b)] acts as a strong perturbation which enlarges the band gap. It opens a finite energy

splitting at the intersection points, defined as the hybridization gap Δ_{hyb} . With a further increase in magnitude to $t_2 = -0.02$ [Fig. 6(c)], the Δ_{hyb} is significantly enlarged. This gap forces the Fermi surface to reconstruct, and the contours of Band 2 and Band 3 move $\Delta_{hyb}e$ farther apart, separating into two distinct closed loops.

To quantify this trend, Figure 6(d) presents a dual-axis plot that tracks the synchronized evolution of the hybridization gap Δ_{hyb} and the momentum separation Δk . We find that both the momentum separation Δk between adjacent orbits and the hybridization gap Δ_{hyb} increase monotonically with increasing t_2 . This behavior demonstrates that t_2 serves as a key control parameter for the gap magnitude, directly enhancing the geometric separation of the coupled orbits.

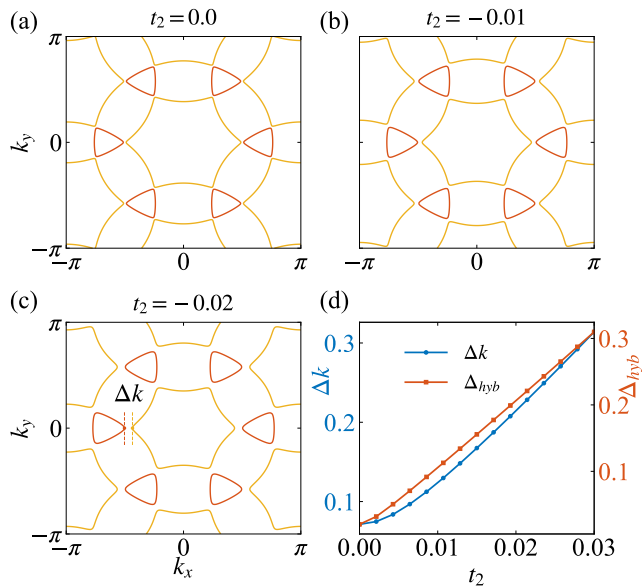


FIG. 6. (Color online) Evolution of the Fermi surface geometry and hybridization gap driven by the next-nearest-neighbor hopping t_2 ($\lambda = 0.05t$). (a)-(c) Fermi surface contours at $E_F = 0$ for (a) $t_2 = 0$, (b) $t_2 = -0.01$, and (c) $t_2 = -0.02$. Increasing t_2 acts as a perturbation that progressively separates Band 2 and Band 3. The momentum separation Δk is explicitly marked in (c). (d) Quantitative dependence of the momentum-space separation Δk (blue circles, left axis) and the hybridization energy gap Δ_{hyb} (red squares, right axis) on t_2 . The monotonic increase of both parameters confirms that t_2 serves as the critical control parameter governing the magnitude of the energy barrier and the geometric separation between the adjacent bands.

In quantum oscillation measurements, the application of strong magnetic fields allows carriers to tunnel across the avoided crossing if the hybridization gap Δ_{hyb} is sufficiently small. This phenomenon, known as magnetic breakdown, leads to the formation of coupled orbits [43]. Consequently, the magnitude of Δ_{hyb} directly dictates the electron dynamics under a magnetic field. The effect of Δ_{hyb} can be quantified by the Blount criterion for magnetic breakdown probability, $P = \exp(-B_0/B)$, where the breakdown field B_0 scales with Δ_{hyb}^2 . As shown in Fig. 7(a), the breakdown probability P is plotted as a function of magnetic field B for different t_2 val-

ues. For small t_2 (e.g., 0.001), breakdown becomes dominant ($P \rightarrow 1$) even at low fields. However, as t_2 increases from 0.001 to 0.015, the breakdown probability decreases clearly. As t_2 increases to 0.015, the breakdown probability is significantly suppressed, reaching only ≈ 0.5 at 50 T. Figure 7(b) further illustrates the sensitivity to t_2 at a fixed experimental field of $B = 35$ T. A sharp transition occurs around $t_2 \approx 0.008$, corresponding to a breakdown probability of $P \approx 0.5$. Below this threshold, P rapidly approaches unity ($P \rightarrow 1$); above it, the probability decreases significantly, indicating a suppression of the magnetic breakdown.

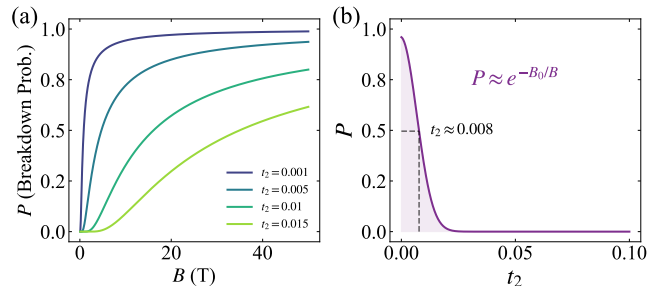


FIG. 7. (Color online) Calculated magnetic breakdown probabilities P based on the Blount criterion $P = \exp(-B_0/B)$, where the breakdown field $B_0 \propto \Delta_{hyb}^2$. (a) Breakdown probability as a function of magnetic field B for various t_2 values. For small t_2 (e.g., 0.001), breakdown occurs even at low fields, whereas for larger t_2 (e.g., 0.015), the breakdown probability is significantly suppressed, reaching only ≈ 0.5 at 50 T. (b) Breakdown probability as a function of t_2 at a fixed experimental field of $B = 35$ T. A sharp transition is observed around $t_2 \approx 0.008$ (where $P \approx 0.5$). Below this threshold, P rapidly approaches unity; above it, the probability decreases significantly, marking the transition to a stable orbit regime.

This distinct dynamical behavior provides a natural explanation for the apparent absence of the topological signal in the case of $t_2 = 0$. Figure 8 visualizes the Berry flux density distribution in momentum space. Theoretically, the geometric phase accumulated along a closed cyclotron orbit C is determined by the total flux of the Berry curvature through the enclosed surface S , as described by Stokes' theorem:

$$\phi_B = \iint_S [\nabla_{\mathbf{k}} \times \mathbf{A}_m(\mathbf{k})] \cdot d\mathbf{S} = \iint_S \boldsymbol{\Omega}_m(\mathbf{k}) \cdot d\mathbf{S} \quad (5)$$

where m represents the band index, $\mathbf{A}_m(\mathbf{k})$ denotes the Berry connection, and $\boldsymbol{\Omega}_m(\mathbf{k})$ is the Berry curvature. The color scale in Fig. 8 represents the z -component of the Berry curvature, $\Omega_z(\mathbf{k}) = \boldsymbol{\Omega}_m(\mathbf{k}) \cdot \hat{z}$, which describes the local contribution to the Berry phase. As shown in the simulation, the Berry curvature is highly concentrated at the gap opening points, referred to as hotspots. For the two adjacent bands (Band 2 and Band 3), the Berry flux density exhibits opposite signs at the hotspots. For the case of $t_2 = 0$, magnetic breakdown allows carriers to easily tunnel across the avoided crossing points, effectively tracing a large quasi-circular orbit that encompasses the coupled trajectories of Band 2 and Band 3. As visualized in Fig. 8(a), the positive and negative Berry curvatures from the two bands cancel each other out during this combined motion.

Consequently, the net Berry phase accumulated over this reconstructed orbit is approximately zero ($\phi_B \approx 0$), accounting for the near-zero intercept observed in RbTi₃Bi₅. Conversely, for $t_2 = -0.01$, magnetic breakdown is suppressed by the large gap. Tunneling to the adjacent band is prohibited, confining carriers to specific stable orbits, such as the triangular orbit of Band 2 shown in Fig. 8(b). This orbit encloses a net non-zero Berry curvature, resulting in a non-trivial phase ($\phi_B \approx \pi$), consistent with the observation in CsTi₃Bi₅.

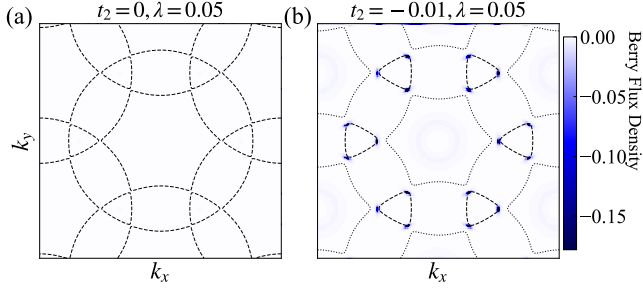


FIG. 8. (Color online) Visualization of Berry flux density distribution. (a) Total Berry flux density of Band 2 and Band 3 at $t_2 = 0$. Due to magnetic breakdown, the electron orbit effectively averages over both bands. The positive and negative Berry curvatures accumulated near the hybridization gaps cancel each other, resulting in a net trivial Berry phase ($\phi_B \approx 0$). (b) Berry flux density of the single Band 2 at $t_2 = -0.01$. The large hybridization gap confines the electron to the Band 2 orbit (dashed line), which encloses a net non-zero Berry curvature, yielding a non-trivial phase ($\phi_B \approx \pi$).

Our analysis establishes a coherent physical picture: The model exhibits non-trivial topology under SOC in both cases. However, under strong magnetic fields, magnetic breakdown significantly influences the quantum oscillation signatures. Crucially, the next-nearest-neighbor hopping t_2 , driven by lattice expansion, acts as a key protective mechanism. By enlarging the hybridization gap, t_2 suppresses magnetic breakdown and prevents tunneling between adjacent bands, thereby making the topological phase experimentally observable in CsTi₃Bi₅.

IV. CONCLUSION

In summary, we establish a unified physical framework to understand the distinct quantum oscillation behaviors in the ATi₃Bi₅ kagome family ($A = \text{Cs, Rb}$). Using a tight-binding model, we capture the essential electronic structure of these materials and reproduce the key experimental features. Our results demonstrate that the next-nearest-neighbor hopping t_2 plays an important role in controlling the quantum oscillation response and the visibility of topological signatures in kagome systems.

Although both RbTi₃Bi₅ and CsTi₃Bi₅ host a nontrivial topology induced by spin-orbit coupling, their Landau fan diagram intercepts exhibit markedly different behaviors. We show that this difference originates from the subtle tuning of the Fermi surface geometry by t_2 , which determines whether the underlying topological information can be accessed in quantum oscillation measurements.

We identify magnetic breakdown as the key filtering mechanism for topological detection. In the Rb-like system ($t_2 = 0$), the hybridization gap is too small to prevent tunneling between adjacent bands under strong magnetic fields. This leads to the cancellation of Berry curvature contributions, making the topological signatures undetectable in quantum oscillation measurements. As a result, the intrinsic topological character becomes invisible in quantum oscillations. In contrast, lattice expansion in the Cs-like system ($t_2 = -0.01$) enhances the hybridization gap and suppresses magnetic breakdown, allowing electrons to remain confined to stable orbits and protecting the intrinsic π Berry phase. More generally, our work highlights hopping engineering as an effective route to control the observability of topological signatures in multiband kagome materials.

ACKNOWLEDGMENTS

This work was supported by the National Natural Science Foundation of China (Grant No.11874139), the Natural Science Foundation of Hebei Province (Grant No.A2019205190), and the Scientific Research Foundation of Hebei Normal University (Grant No.L2024J02).

Appendix A: Explicit Matrix Form of the Hamiltonian for Band Structure Calculations

The tight-binding model presented in the main text is derived from real-space hopping integrals. For the numerical calculation of band structures and Fermi surfaces presented in Figs. 2, 5, and 6, we utilize a symmetrized momentum-space representation. This form is obtained by a gauge transformation that absorbs the phase factors $e^{i\mathbf{k}\cdot\mathbf{d}/2}$ into the basis states, resulting in a Hamiltonian expressed in terms of cosine functions.

The basis is defined as $\Psi_{\mathbf{k}}^\dagger = (c_{1\mathbf{k}}^\dagger, c_{2\mathbf{k}}^\dagger, c_{3\mathbf{k}}^\dagger, c_{4\mathbf{k}}^\dagger)$. The total Hamiltonian in momentum space corresponds to Eq. (1) in the main text:

$$H(\mathbf{k}) = H_0(\mathbf{k}) + H_{\text{SOC}}(\mathbf{k}). \quad (\text{A1})$$

The first term, $H_0(\mathbf{k})$, represents the spin-independent hopping processes (corresponding to Eq. (2)). It is a real symmetric matrix given by:

$$H_0(\mathbf{k}) = -2 \begin{pmatrix} 0 & t \cos(k_1) & t \cos(k_2) & t_1 \cos(k_3) + t_2 \cos(k_5) \\ t \cos(k_1) & 0 & t \cos(k_3) & t_1 \cos(k_2) + t_2 \cos(k_6) \\ t \cos(k_2) & t \cos(k_3) & 0 & t_1 \cos(k_1) + t_2 \cos(k_4) \\ t_1 \cos(k_3) + t_2 \cos(k_5) & t_1 \cos(k_2) + t_2 \cos(k_6) & t_1 \cos(k_1) + t_2 \cos(k_4) & 0 \end{pmatrix}, \quad (\text{A2})$$

where the lower triangle elements are determined by hermiticity (symmetry).

The second term, $H_{\text{SOC}}(\mathbf{k})$, represents the spin-orbit coupling (corresponding to Eq. (3)). It is a purely imaginary Hermitian matrix given by:

$$H_{\text{SOC}}(\mathbf{k}) = 2i\lambda \begin{pmatrix} 0 & \cos(k_2 + k_3) & -\cos(k_3 - k_1) & 0 \\ -\cos(k_2 + k_3) & 0 & \cos(k_1 + k_2) & 0 \\ \cos(k_3 - k_1) & -\cos(k_1 + k_2) & 0 & 0 \\ 0 & 0 & 0 & 0 \end{pmatrix}. \quad (\text{A3})$$

The momentum coordinates k_i are defined as linear combinations of k_x and k_y , projecting the momentum along the lattice bond directions:

$$\begin{aligned} k_1 &= k_x, & k_4 &= \sqrt{3}k_y, \\ k_2 &= \frac{1}{2}k_x + \frac{\sqrt{3}}{2}k_y, & k_5 &= -\frac{3}{2}k_x - \frac{\sqrt{3}}{2}k_y, \\ k_3 &= -\frac{1}{2}k_x + \frac{\sqrt{3}}{2}k_y, & k_6 &= \frac{3}{2}k_x - \frac{\sqrt{3}}{2}k_y. \end{aligned}$$

This separation into H_0 and H_{SOC} clearly illustrates that the hopping terms are even functions of \mathbf{k} (preserving time-reversal symmetry in the absence of SOC), while the SOC terms introduce the necessary chirality to open the topological gap.

Appendix B: Green's Function Formalism and Numerical Implementation

To compute the density of states at the Fermi energy, we employ the recursive Green's function algorithm, which efficiently evaluates the diagonal blocks of the retarded Green's function

$$G^r(E) = (E - H + i\eta)^{-1}. \quad (\text{B1})$$

The method propagates layer by layer through the discretized lattice structure of the system, as illustrated schematically in Fig. 9. The overall procedure consists of three steps: initialization of boundary Green's functions, recursive propagation from both ends of the system toward the center, and final combination at the central layer.

We begin by initializing the boundary Green's functions for the left and right surfaces, which serve as starting points of the recursion:

$$G_{SS}^r = (E - H_{00} - \Sigma_L)^{-1}, \quad (\text{B2})$$

$$G_{TT}^r = (E - H_{00} - \Sigma_R)^{-1}, \quad (\text{B3})$$

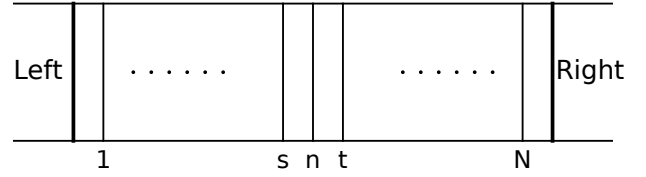


FIG. 9. (Color online) Schematic illustration of the recursive Green's function algorithm for layered systems. The calculation proceeds from both boundaries toward the center: (i) initialization of the left surface Green's function G_{SS}^r , (ii) initialization of the right surface Green's function G_{TT}^r , (iii) left-to-right recursive propagation (red arrows), (iv) right-to-left recursive propagation (blue arrows), (v) final combination at the center layer n to obtain G_{nn}^r . This algorithm avoids full matrix inversion by exploiting the layered structure.

where the self-energies $\Sigma_{L(R)}$ are set to zero to enforce open boundary conditions.

Starting from the left surface Green's function G_{SS}^r , we propagate toward the center using

$$G_{ss}^r = \left(E - H_{00} - H_{01}^\dagger G_{ss}^r H_{01} \right)^{-1}. \quad (\text{B4})$$

Similarly, propagation from the right surface yields

$$G_{tt}^r = \left(E - H_{00} - H_{01} G_{tt}^r H_{01}^\dagger \right)^{-1}. \quad (\text{B5})$$

The Green's function of the central layer is then obtained by combining the left and right propagated results:

$$G_{nn}^r = \left(E - H_{00} - H_{01}^\dagger G_{ss}^r H_{01} - H_{01} G_{tt}^r H_{01}^\dagger \right)^{-1}. \quad (\text{B6})$$

From this expression, the layer-resolved DOS at the Fermi energy follows as

$$D_n(\epsilon_F) = -\frac{1}{\pi} \text{Im} \text{Tr}[G_{nn}^r(\epsilon_F)]. \quad (\text{B7})$$

Appendix C: Thermodynamic Damping and Effective Mass Analysis

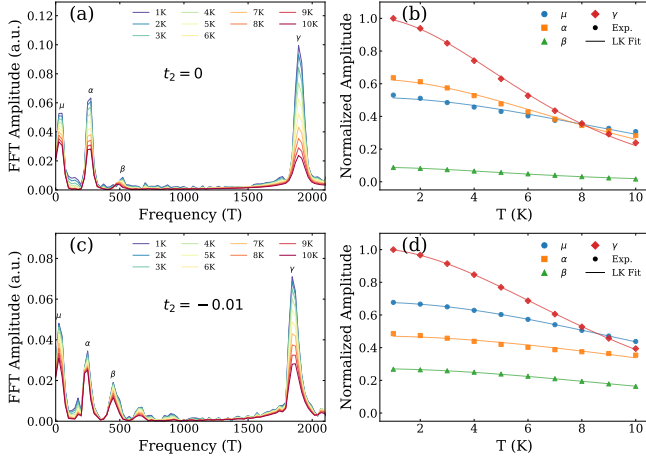


FIG. 10. (Color online) Temperature dependence of quantum oscillation amplitudes and effective mass extraction for the kagome lattice model with spin-orbit coupling $\lambda = 0.05t$. (a, c) Fast Fourier Transform (FFT) amplitude spectra for the cases of $t_2 = 0$ [(a)] and $t_2 = -0.02$ [(c)], with temperatures varying from 1.00 K (purple) to 10.00 K (red). The dominant fundamental frequencies are labeled. (b, d) Temperature dependence of the normalized FFT amplitudes (symbols) for the corresponding frequency peaks. The solid lines represent fits to the Lifshitz-Kosevich (LK) formula, from which the effective masses m^* (in units of m_0) are extracted for $t_2 = 0$ [(b)] and $t_2 = -0.01$ [(d)].

In this appendix, we provide the theoretical background for the temperature effects on quantum oscillations and detail the extraction of effective masses for the two lattice cases discussed in the main text.

At finite temperatures, the oscillatory component of the density of states (DOS) is thermally broadened, a phenomenon described by the standard Lifshitz-Kosevich (LK) theory. Mathematically, the temperature-dependent DOS, $D(E, T)$, is obtained by convolving the zero-temperature DOS, $D(E)$, with the derivative of the Fermi-Dirac distribution function:

$$D(\mu, T) = \int_{-\infty}^{+\infty} dE \left(-\frac{\partial n_F(E, T)}{\partial E} \right) D(E), \quad (\text{C1})$$

where $n_F(E, T) = [e^{(E-\mu)/k_B T} + 1]^{-1}$ is the Fermi-Dirac distribution, with k_B being the Boltzmann constant and μ the chemical potential. The thermal kernel $-\partial n_F/\partial E$ broadens the Fermi surface singularity, thereby reducing the amplitude of quantum oscillations as temperature increases.

To quantify this damping effect in our kagome models, we performed calculations at finite temperatures for both the $t_2 = 0$ (Rb-like) and $t_2 = -0.01$ (Cs-like) cases, with a fixed spin-orbit coupling $\lambda = 0.05t$. The results are summarized in

Fig. 10. As shown in Figs. 10(a) and 10(c), the corresponding Fast Fourier Transform (FFT) spectra identify the fundamental frequencies (labeled μ , α , β , and γ).

By tracking the temperature dependence of the FFT amplitudes [Figs. 10(b) and 10(d)], we extract the carrier effective masses using the LK amplitude formula:

$$\mathcal{A}(T) \propto \frac{X}{\sinh(X)}, \quad \text{where } X = \frac{\alpha m^* T}{B}, \quad (\text{C2})$$

with $\alpha \approx 14.69$ T/K and B denoting the average magnetic field.

The extracted effective masses (in units of the free electron mass m_0) reveal a distinct renormalization effect driven by the hopping integrals. For the $t_2 = 0$ case, the effective masses are $m_\mu^* \approx 0.445$, $m_\alpha^* \approx 0.567$, $m_\beta^* \approx 0.788$, and $m_\gamma^* \approx 0.783$. In contrast, introducing the next-nearest-neighbor hopping ($t_2 = -0.01$) generally reduces the effective masses to $m_\mu^* \approx 0.386$, $m_\alpha^* \approx 0.332$, $m_\beta^* \approx 0.414$, and $m_\gamma^* \approx 0.594$.

Physically, this reduction in effective mass arises from the modification of the band dispersion by t_2 , which increases the Fermi velocity for most orbital trajectories. All extracted masses satisfy $m^* < m_0$, consistent with the high-mobility character observed experimentally in these kagome metals. The excellent agreement between our numerical data and the LK fits confirms that our tight-binding model correctly captures the quasiparticle dynamics near the Fermi level.

Appendix D: Determination of Berry Phase from Landau Fan Diagram

The Berry phase is extracted from the Landau fan diagram constructed using the oscillatory extrema of the DOS. Maxima (peaks) are assigned half-integer Landau indices, while minima (valleys) correspond to integer indices. The oscillatory DOS is approximately described by

$$\text{DOS} \propto R_T R_D \cos \left[2\pi \left(\frac{F}{B} - \frac{1}{2} + \frac{\phi_B}{2\pi} \right) \right], \quad (\text{D1})$$

where R_T and R_D are the temperature and Dingle damping factors, F is the oscillation frequency, B is the magnetic field, and ϕ_B is the Berry phase. The Lifshitz-Onsager relation then connects the Landau index N with the inverse magnetic field:

$$N = \frac{F}{B} + \frac{\phi_B}{2\pi}. \quad (\text{D2})$$

By plotting N versus $1/B$, the Landau fan diagram is obtained, and the intercept yields $\phi_B/2\pi$. For Dirac-like carriers characterized by a non-trivial Berry phase of π , the intercept is expected to be near 0.5. In contrast, an intercept close to zero corresponds to a trivial Berry phase. In our calculation, the extracted intercept is 0.047 (see Fig. 3(c) of the main text), implying a Berry phase close to zero and confirming the trivial topological nature of the electronic states.

- [1] W.-S. Wang, Z.-Z. Li, Y.-Y. Xiang, and Q.-H. Wang, Competing electronic orders on kagome lattices at van hove filling, *Phys. Rev. B* **87**, 115135 (2013).
- [2] L.-K. Lim, J.-N. Fuchs, F. Piéchon, and G. Montambaux, Dirac points emerging from flat bands in lieb-kagome lattices, *Phys. Rev. B* **101**, 045131 (2020).
- [3] M. Li, Q. Wang, G. Wang, Z. Yuan, W. Song, R. Lou, Z. Liu, Y. Huang, Z. Liu, H. Lei, Z. Yin, and S. Wang, Dirac cone, flat band and saddle point in kagome magnet YMn_6Sn_6 , *Nature Communications* **12**, 3129 (2021).
- [4] M. Kang, L. Ye, S. Fang, J.-S. You, A. Levitan, M. Han, J. I. Facio, C. Jozwiak, A. Bostwick, E. Rotenberg, M. K. Chan, R. D. McDonald, D. Graf, K. Kaznatcheev, E. Vescovo, D. C. Bell, E. Kaxiras, J. van den Brink, M. Richter, M. Prasad Ghimire, J. G. Checkelsky, and R. Comin, Dirac fermions and flat bands in the ideal kagome metal FeSn , *Nature Materials* **19**, 163 (2020).
- [5] J.-X. Yin, B. Lian, and M. Z. Hasan, Topological kagome magnets and superconductors, *Nature* **612**, 647 (2022).
- [6] K. Shrestha, R. Chapai, B. K. Pokharel, D. Miertschin, T. Nguyen, X. Zhou, D. Y. Chung, M. G. Kanatzidis, J. F. Mitchell, U. Welp, D. Popović, D. E. Graf, B. Lorenz, and W. K. Kwok, Nontrivial fermi surface topology of the kagome superconductor CsV_3Sb_5 probed by de haas–van alphen oscillations, *Phys. Rev. B* **105**, 024508 (2022).
- [7] Y. Fu, N. Zhao, Z. Chen, Q. Yin, Z. Tu, C. Gong, C. Xi, X. Zhu, Y. Sun, K. Liu, and H. Lei, Quantum transport evidence of topological band structures of kagome superconductor CsV_3Sb_5 , *Phys. Rev. Lett.* **127**, 207002 (2021).
- [8] R. Chapai, M. Leroux, V. Oliviero, D. Vignolles, N. Bruyant, M. P. Smylie, D. Y. Chung, M. G. Kanatzidis, W.-K. Kwok, J. F. Mitchell, and U. Welp, Magnetic breakdown and topology in the kagome superconductor CsV_3Sb_5 under high magnetic field, *Phys. Rev. Lett.* **130**, 126401 (2023).
- [9] X. Huang, C. Guo, C. Putzke, M. Gutierrez-Amigo, Y. Sun, M. G. Vergniory, I. Errea, D. Chen, C. Felser, and P. J. W. Moll, Three-dimensional fermi surfaces from charge order in layered CsV_3Sb_5 , *Phys. Rev. B* **106**, 064510 (2022).
- [10] Z. Liang, X. Hou, F. Zhang, W. Ma, P. Wu, Z. Zhang, F. Yu, J.-J. Ying, K. Jiang, L. Shan, Z. Wang, and X.-H. Chen, Three-dimensional charge density wave and surface-dependent vortex-core states in a kagome superconductor CsV_3Sb_5 , *Phys. Rev. X* **11**, 031026 (2021).
- [11] B. R. Ortiz, L. C. Gomes, J. R. Morey, M. Winiarski, M. Bordelon, J. S. Mangum, I. W. H. Oswald, J. A. Rodriguez-Rivera, J. R. Neilson, S. D. Wilson, E. Ertekin, T. M. McQueen, and E. S. Toberer, New kagome prototype materials: discovery of KV_3Sb_5 , RbV_3Sb_5 , and CsV_3Sb_5 , *Phys. Rev. Mater.* **3**, 094407 (2019).
- [12] H. Tan, Y. Liu, Z. Wang, and B. Yan, Charge density waves and electronic properties of superconducting kagome metals, *Phys. Rev. Lett.* **127**, 046401 (2021).
- [13] C. Broyles, D. Graf, H. Yang, X. Dong, H. Gao, and S. Ran, Effect of the interlayer ordering on the fermi surface of kagome superconductor CsV_3Sb_5 revealed by quantum oscillations, *Phys. Rev. Lett.* **129**, 157001 (2022).
- [14] B. R. Ortiz, S. M. L. Teicher, L. Kautzsch, P. M. Sarte, N. Ratcliff, J. Harter, J. P. C. Ruff, R. Seshadri, and S. D. Wilson, Fermi surface mapping and the nature of charge-density-wave order in the kagome superconductor CsV_3Sb_5 , *Phys. Rev. X* **11**, 041030 (2021).
- [15] H. Li, H. Zhao, B. R. Ortiz, Y. Oey, Z. Wang, S. D. Wilson, and I. Zeljkovic, Unidirectional coherent quasiparticles in the high-temperature rotational symmetry broken phase of AV_3Sb_5 kagome superconductors, *Nature Physics* **19**, 637 (2023).
- [16] Y.-X. Jiang, J.-X. Yin, M. M. Denner, N. Shumiya, B. R. Ortiz, G. Xu, Z. Guguchia, J. He, M. S. Hossain, X. Liu, J. Ruff, L. Kautzsch, S. S. Zhang, G. Chang, I. Belopolski, Q. Zhang, T. A. Cochran, D. Multer, M. Litskevich, Z.-J. Cheng, X. P. Yang, Z. Wang, R. Thomale, T. Neupert, S. D. Wilson, and M. Z. Hasan, Unconventional chiral charge order in kagome superconductor KV_3Sb_5 , *Nature Materials* **20**, 1353 (2021).
- [17] B. Hu, Y. Ye, Z. Huang, X. Han, Z. Zhao, H. Yang, H. Chen, and H.-J. Gao, Robustness of the unidirectional stripe order in the kagome superconductor CsV_3Sb_5 , *Chin. Phys. B* **31**, 058102 (2022).
- [18] B. R. Ortiz, S. M. L. Teicher, Y. Hu, J. L. Zuo, P. M. Sarte, E. C. Schueller, A. M. M. Abeykoon, M. J. Krogstad, S. Rosenkranz, R. Osborn, R. Seshadri, L. Balents, J. He, and S. D. Wilson, CsV_3Sb_5 : A \mathbb{Z}_2 topological kagome metal with a superconducting ground state, *Phys. Rev. Lett.* **125**, 247002 (2020).
- [19] H. Li, T. T. Zhang, T. Yilmaz, Y. Y. Pai, C. E. Marvinney, A. Said, Q. W. Yin, C. S. Gong, Z. J. Tu, E. Vescovo, C. S. Nelson, R. G. Moore, S. Murakami, H. C. Lei, H. N. Lee, B. J. Lawrie, and H. Miao, Observation of unconventional charge density wave without acoustic phonon anomaly in kagome superconductors AV_3Sb_5 ($A=\text{Rb}, \text{Cs}$), *Phys. Rev. X* **11**, 031050 (2021).
- [20] S. Cho, H. Ma, W. Xia, Y. Yang, Z. Liu, Z. Huang, Z. Jiang, X. Lu, J. Liu, Z. Liu, J. Li, J. Wang, Y. Liu, J. Jia, Y. Guo, J. Liu, and D. Shen, Emergence of new van hove singularities in the charge density wave state of a topological kagome metal RbV_3Sb_5 , *Phys. Rev. Lett.* **127**, 236401 (2021).
- [21] J. Zhao, W. Wu, Y. Wang, and S. A. Yang, Electronic correlations in the normal state of the kagome superconductor KV_3Sb_5 , *Phys. Rev. B* **103**, L241117 (2021).
- [22] K. Nakayama, Y. Li, T. Kato, M. Liu, Z. Wang, T. Takahashi, Y. Yao, and T. Sato, Multiple energy scales and anisotropic energy gap in the charge-density-wave phase of the kagome superconductor CsV_3Sb_5 , *Phys. Rev. B* **104**, L161112 (2021).
- [23] T. Qian, M. H. Christensen, C. Hu, A. Saha, B. M. Andersen, R. M. Fernandes, T. Birol, and N. Ni, Revealing the competition between charge density wave and superconductivity in CsV_3Sb_5 through uniaxial strain, *Phys. Rev. B* **104**, 144506 (2021).
- [24] F. H. Yu, D. H. Ma, W. Z. Zhuo, S. Q. Liu, X. K. Wen, B. Lei, J. J. Ying, and X. H. Chen, Unusual competition of superconductivity and charge-density-wave state in a compressed topological kagome metal, *Nature Communications* **12**, 3645 (2021).
- [25] K. Y. Chen, N. N. Wang, Q. W. Yin, Y. H. Gu, K. Jiang, Z. J. Tu, C. S. Gong, Y. Uwatoko, J. P. Sun, H. C. Lei, J. P. Hu, and J.-G. Cheng, Double superconducting dome and triple enhancement of T_c in the kagome superconductor CsV_3Sb_5 under high pressure, *Phys. Rev. Lett.* **126**, 247001 (2021).
- [26] Q. Wang, P. Kong, W. Shi, C. Pei, C. Wen, L. Gao, Y. Zhao, Q. Yin, Y. Wu, G. Li, H. Lei, J. Li, Y. Chen, S. Yan, and Y. Qi, Charge density wave orders and enhanced superconductivity under pressure in the kagome metal CsV_3Sb_5 , *Advanced Materials* **33**, 2102813 (2021).
- [27] N. Shumiya, M. S. Hossain, J.-X. Yin, Y.-X. Jiang, B. R. Ortiz, H. Liu, Y. Shi, Q. Yin, H. Lei, S. S. Zhang, G. Chang, Q. Zhang, T. A. Cochran, D. Multer, M. Litskevich, Z.-J. Cheng, X. P. Yang, Z. Guguchia, S. D. Wilson, and M. Z. Hasan, Intrinsic

- sic nature of chiral charge order in the kagome superconductor RbV_3Sb_5 , *Phys. Rev. B* **104**, 035131 (2021).
- [28] Z. Wang, Y.-X. Jiang, J.-X. Yin, Y. Li, G.-Y. Wang, H.-L. Huang, S. Shao, J. Liu, P. Zhu, N. Shumiya, M. S. Hossain, H. Liu, Y. Shi, J. Duan, X. Li, G. Chang, P. Dai, Z. Ye, G. Xu, Y. Wang, H. Zheng, J. Jia, M. Z. Hasan, and Y. Yao, Electronic nature of chiral charge order in the kagome superconductor CsV_3Sb_5 , *Phys. Rev. B* **104**, 075148 (2021).
- [29] F. H. Yu, T. Wu, Z. Y. Wang, B. Lei, W. Z. Zhuo, J. J. Ying, and X. H. Chen, Concurrence of anomalous hall effect and charge density wave in a superconducting topological kagome metal, *Phys. Rev. B* **104**, L041103 (2021).
- [30] D. Chen, B. He, M. Yao, Y. Pan, H. Lin, W. Schnelle, Y. Sun, J. Gooth, L. Taillefer, and C. Felser, Anomalous thermoelectric effects and quantum oscillations in the kagome metal CsV_3Sb_5 , *Phys. Rev. B* **105**, L201109 (2022).
- [31] W. Zhang, L. Wang, C. W. Tsang, X. Liu, J. Xie, W. C. Yu, K. T. Lai, and S. K. Goh, Emergence of large quantum oscillation frequencies in thin flakes of the kagome superconductor CsV_3Sb_5 , *Phys. Rev. B* **106**, 195103 (2022).
- [32] C. Yi, X. Feng, N. Mao, P. Yanda, S. Roychowdhury, Y. Zhang, C. Felser, and C. Shekhar, Quantum oscillations revealing topological band in kagome metal ScV_6Sn_6 , *Phys. Rev. B* **109**, 035124 (2024).
- [33] D. Werhahn, B. R. Ortiz, A. K. Hay, S. D. Wilson, R. Seshadri, and D. Johrendt, The kagome metals RbTi_3Bi_5 and CsTi_3Bi_5 , *Z. Naturforsch. B* **77**, 757 (2022).
- [34] H. Li, S. Cheng, B. R. Ortiz, H. Tan, D. Werhahn, K. Zeng, D. Johrendt, B. Yan, Z. Wang, S. D. Wilson, and I. Zeljkovic, Electronic nematicity without charge density waves in titanium-based kagome metal (2023), [arXiv:2211.16477](https://arxiv.org/abs/2211.16477) [cond-mat.str-el].
- [35] X.-W. Yi, X.-Y. Ma, Z. Zhang, Z.-W. Liao, J.-Y. You, and G. Su, Large kagome family candidates with topological superconductivity and charge density waves, *Phys. Rev. B* **106**, L220505 (2022).
- [36] Y. Wang, Y. Liu, Z. Hao, W. Cheng, J. Deng, Y. Wang, Y. Gu, X.-M. Ma, H. Rong, F. Zhang, S. Guo, C. Zhang, Z. Jiang, Y. Yang, W. Liu, Q. Jiang, Z. Liu, M. Ye, D. Shen, Y. Liu, S. Cui, L. Wang, C. Liu, J. Lin, Y. Liu, Y. Cai, J. Zhu, C. Chen, and J.-W. Mei, Flat band and \mathbb{Z}_2 topology of kagome metal CsTi_3Bi_5 , *Chin. Phys. Lett.* **40**, 037102 (2023).
- [37] Y. Zhou, L. Chen, X. Ji, C. Liu, K. Liao, Z. Guo, J. Wang, H. Weng, and G. Wang, [Physical properties, electronic structure, and strain-tuned monolayer of the weak topological insulator \$\text{RbTi}_3\text{Bi}_5\$ with kagome lattice](https://arxiv.org/abs/2301.01633) (2023), [arXiv:2301.01633](https://arxiv.org/abs/2301.01633) [cond-mat.supr-con].
- [38] T.-M. Chuang, M. P. Allan, J. Lee, Y. Xie, N. Ni, S. L. Bud'ko, G. S. Boebinger, P. C. Canfield, and J. C. Davis, Nematic electronic structure, *Science* **327**, 181 (2010).
- [39] Y. Li, H. Tan, and B. Yan, [Quantum oscillations with topological phases in a kagome metal \$\text{CsTi}_3\text{Bi}_5\$](https://arxiv.org/abs/2307.04750) (2023), [arXiv:2307.04750](https://arxiv.org/abs/2307.04750) [cond-mat.str-el].
- [40] A. López-Martínez, [Recurrent subspaces in banach spaces](https://arxiv.org/abs/2212.04464) (2024), [arXiv:2212.04464](https://arxiv.org/abs/2212.04464) [math.FA].
- [41] Y. Li, Q. Li, X. Fan, J. Liu, Q. Feng, M. Liu, C. Wang, J.-X. Yin, J. Duan, X. Li, Z. Wang, H.-H. Wen, and Y. Yao, Tuning the competition between superconductivity and charge order in the kagome superconductor $\text{Cs}(\text{V}_{1-x}\text{Nb}_x)_3\text{Sb}_5$, *Phys. Rev. B* **105**, L180507 (2022).
- [42] Z. Rehffuss, C. Broyles, D. Graf, Y. Li, H. Tan, Z. Zhao, J. Liu, Y. Zhang, X. Dong, H. Yang, H. Gao, B. Yan, and S. Ran, Quantum oscillations in kagome metals CsTi_3Bi_5 and RbTi_3Bi_5 , *Phys. Rev. Mater.* **8**, 024003 (2024).
- [43] D. Shoenberg, *Magnetic Oscillations in Metals*, Cambridge Monographs on Physics (Cambridge University Press, 1984).
- [44] J. Yang, X. Yi, Z. Zhao, Y. Xie, T. Miao, H. Luo, H. Chen, B. Liang, W. Zhu, Y. Ye, J.-Y. You, B. Gu, S. Zhang, F. Zhang, F. Yang, Z. Wang, Q. Peng, H. Mao, G. Liu, Z. Xu, H. Chen, H. Yang, G. Su, H. Gao, L. Zhao, and X. J. Zhou, Observation of flat band, Dirac nodal lines and topological surface states in Kagome superconductor CsTi_3Bi_5 , *Nature Communications* **14**, 4089 (2023).
- [45] Z. Jiang, Z. Liu, H. Ma, W. Xia, Z. Liu, J. Liu, S. Cho, Y. Yang, J. Ding, J. Liu, Z. Huang, Y. Qiao, J. Shen, W. Jing, X. Liu, J. Liu, Y. Guo, and D. Shen, Flat bands, non-trivial band topology and rotation symmetry breaking in layered kagome-lattice RbTi_3Bi_5 , *Nature Communications* **14**, 4892 (2023).
- [46] H.-M. Guo and M. Franz, Topological insulator on the kagome lattice, *Physical Review B* **80**, 113102 (2009).
- [47] L. Zhang, X.-Y. Song, and F. Wang, Quantum Oscillation in Narrow-Gap Topological Insulators, *Physical Review Letters* **116**, 046404 (2016).
- [48] J. Song, H. Liu, J. Liu, Y.-X. Li, R. Joynt, Q.-f. Sun, and X. C. Xie, Quantum interference in topological insulator josephson junctions, *Phys. Rev. B* **93**, 195302 (2016).
- [49] L. Zhang and J.-W. Mei, [Reconstructed fermi surface and quantum oscillation of doped resonating valence bond state with incommensurate charge order in underdoped cuprates](https://arxiv.org/abs/1408.6592) (2015), [arXiv:1408.6592](https://arxiv.org/abs/1408.6592) [cond-mat.supr-con].
- [50] J.-c. Chen, J. Wang, and Q.-f. Sun, Effect of magnetic field on electron transport in HgTe/CdTe quantum wells: Numerical analysis, *Phys. Rev. B* **85**, 125401 (2012).
- [51] L. Du, Q. Chen, A. D. Barr, A. R. Barr, and G. A. Fiete, Floquet hofstadter butterfly on the kagome and triangular lattices, *Phys. Rev. B* **98**, 245145 (2018).
- [52] A. Avsar, H. Ochoa, F. Guinea, B. Özyilmaz, B. J. Van Wees, and I. J. Vera-Marun, *Colloquium*: Spintronics in graphene and other two-dimensional materials, *Reviews of Modern Physics* **92**, 021003 (2020).
- [53] C.-Z. Chen, J. Song, H. Jiang, Q.-f. Sun, Z. Wang, and X. C. Xie, Disorder and Metal-Insulator Transitions in Weyl Semimetals, *Physical Review Letters* **115**, 246603 (2015).
- [54] J. Li, R.-L. Chu, J. K. Jain, and S.-Q. Shen, Topological Anderson Insulator, *Physical Review Letters* **102**, 136806 (2009).
- [55] C. W. Groth, M. Wimmer, A. R. Akhmerov, J. Tworzydło, and C. W. J. Beenakker, Theory of the Topological Anderson Insulator, *Physical Review Letters* **103**, 196805 (2009).
- [56] J. Song, H. Liu, H. Jiang, Q.-f. Sun, and X. C. Xie, Dependence of topological Anderson insulator on the type of disorder, *Physical Review B* **85**, 195125 (2012).
- [57] F. D. M. Haldane, Model for a Quantum Hall Effect without Landau Levels: Condensed-Matter Realization of the “parity anomaly”, *Physical Review Letters* **61**, 2015 (1988).